

---

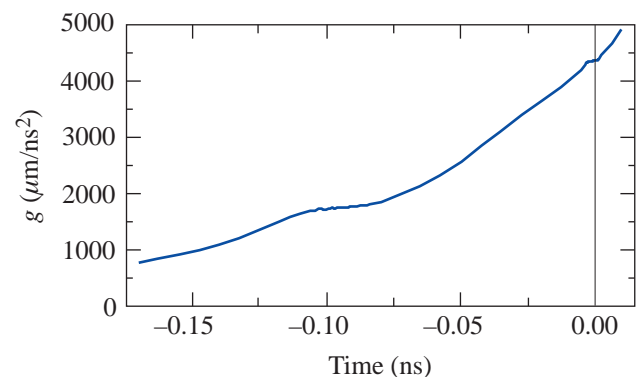
# Theory of the Hot-Spot Dynamics and Deceleration-Phase Instability of Imploding ICF Capsules

## Introduction

In inertial confinement fusion<sup>1</sup> (ICF), a spherical shell of cryogenic deuterium and tritium (DT) filled with DT gas is accelerated by direct laser irradiation (direct drive) or x-rays produced by a high-Z enclosure (indirect drive). In direct-drive ICF, the laser pulse starts from a constant, low-intensity foot designed to drive a uniform shock through the shell. After the shock breaks out on the shell's inner surface, the latter expands forward, launching a shock in the gas and a rarefaction wave in the shell. As the rarefaction wave travels across the shell, the shell's outer surface moves at approximately constant velocity. When the rarefaction wave reaches the shell's outer surface, the latter starts accelerating and the so-called *acceleration phase* begins. At about the shock breakout time, the laser power begins to rise, first slowly and then more rapidly to keep the shell close to the shock front traveling inside the gas. A second shock originating within the shell is launched during the initial pulse rise and merges with the first shock before reaching the center of the capsule. The acceleration phase ends when the laser is turned off and the shell starts traveling at approximately constant velocity. Standard direct-drive pulse designs make use of such a sequence of two shocks merging into one, whereas the latest pulse designs of indirect-drive ICF make use of a sequence of four shocks<sup>2</sup> coalescing into one before reaching the center.

In both direct- and indirect-drive ICF, the single shock resulting from the multiple-shock coalescence travels in the gas in the form of a *strong* shock; i.e.,  $\Delta P/P_b \gg 1$ , where  $\Delta P$  is the pressure jump across the shock and  $P_b$  is the gas pressure before the shock. Such a shock is reflected off the center of the capsule (return shock) and subsequently off the incoming inner shell surface, which in turn is impulsively decelerated. The shock reflected off the shell travels toward the center, where it is reflected again and subsequently reflected a second time from the shell. At each reflection off the shell, the latter is impulsively decelerated and the shock gets weaker until the pressure jump across the shock front is smaller than the pressure before the shock ( $\Delta P/P_b < 1$ ). The time interval corresponding to the multiple shock reflections is referred to as

the *impulsive deceleration phase*. Typically, the reflected shock becomes *weak* after the first or second reflection off the shell. At this point the material enclosed by the inner shell surface develops a fairly uniform pressure profile and is referred to as the *hot spot*. After the return shock reflects off the shell, the hot spot is formed, and its pressure is large enough that the shell velocity is lower than the hot-spot sound speed, i.e., the flow is subsonic. When the hot spot is formed, the shell is decelerated in a continuous (not impulsive) manner while acting like a piston on the hot spot. Such a continuous slowing down of the shell up to the stagnation point occurs over a period of a few hundred picoseconds and is referred to as the *continuous deceleration phase*. Figure 85.1 shows the time evolution of the deceleration  $g$  of a shell designed for direct-drive ignition<sup>3</sup> on the National Ignition Facility (NIF). The time  $t = 0$  ns represents the stagnation point, and the continuous deceleration starts at about 200 ps before stagnation. The NIF capsule is a 345- $\mu\text{m}$ -thick shell of DT ice with an inner radius of 1350  $\mu\text{m}$ . The shell is filled with DT gas at a temperature of 18 K and a density of  $2 \times 10^{-4}$  g/cm<sup>3</sup>. During the deceleration phase, the hot-spot pressure, density, and temperature increase until reaching the ignition conditions. If the shell is sufficiently dense, the ignited hot spot will trigger a propagating burn wave



TC5421

Figure 85.1  
Time evolution of the inner-shell-surface deceleration for a direct-drive NIF capsule. Time  $t = 0$  is the stagnation time.

in the shell and a significant fraction of the shell mass will undergo thermonuclear burn if the shell's areal density exceeds a few  $\text{g/cm}^2$ .

It is well known that the outer shell surface is unstable to the Rayleigh–Taylor (RT) instability during the acceleration phase; however, because of mass ablation, the instability growth rates are significantly reduced<sup>4–10</sup> with respect to their classical values. The theory of the RT instability in an accelerated planar foil has been carried out in Refs. 6–9, where the growth rate's dependence on the ablation velocity  $V_a$ , density-gradient scale length  $L_m = \min[\rho(\rho')^{-1}]$ , front acceleration  $g$ , and power index for thermal conduction  $\nu$  (here the thermal conductivity is approximated by  $\kappa \approx \kappa_0 T^\nu$ ) is calculated by analytically solving the conservation equations. In Refs. 6–9, the stability of long ( $kL_m < 1$ ) and short ( $kL_m > 1$ ) wavelength modes is investigated for large and small Froude numbers ( $Fr$ ), where  $Fr = V_a^2/gL_0$  and  $L_0 = L_m \nu^\nu / (\nu + 1)^{\nu+1}$ . It is found that short-wavelength modes are completely suppressed when  $Fr > 1$  and the unstable spectrum exhibits a cutoff at long wavelengths, i.e.,  $k_{\text{cutoff}} L_m < 1$ . Instead, when  $Fr < 1$ , the cutoff occurs at short wavelengths ( $k_{\text{cutoff}} L_m \sim 1/Fr^{1/3}$ ), and both long- and short-wavelength modes (up to the cutoff) are unstable. The stability analysis in Refs. 8 and 9 has been carried out separately for large and small Froude numbers as well as long and short wavelengths. In Ref. 10 the different growth-rate solutions have been combined into a single formula that asymptotically matches those solutions in the different parameter ranges.

Despite the significant growth-rate reduction induced by mass ablation and finite-density-gradient scale-length effects, the amplification of surface perturbations can be substantial, so the thickness of ICF shells must be chosen to prevent the shell from breaking up when the RT bubble amplitude equals the shell thickness.

Even when the shell integrity is preserved during the acceleration phase, the hot-spot ignition can be quenched<sup>11</sup> by the deceleration-phase RT instability. The latter is the instability of the inner shell surface that occurs when the shell is decelerated by the high pressure building up inside the hot spot. The deceleration-phase RT causes the cold shell material to penetrate and cool the hot spot, preventing it from achieving ignition conditions. Furthermore, if the inner-surface perturbation becomes nonlinear, a fraction of the shell's kinetic energy is used to feed the lateral shell motion induced by the instability, reducing the compression of the hot spot. Typical seeds for the deceleration-phase RT are the surface nonuniformities that

feed through the shell from the outer surface during the acceleration-phase instability.

It is known that the deceleration-phase RT is classical<sup>12</sup> and all modes are unstable. The finite-density-gradient scale length<sup>13</sup> reduces the instability growth rates, which can be approximated by the classical fitting formula<sup>1</sup>

$$\gamma_{\text{dec}} \approx \sqrt{\frac{kg}{1+kL}}, \quad (1)$$

where  $L$  is the shell's density-gradient scale length and  $k$  is the perturbation wave number approximately equal to  $l/R$  with  $R$  being the hot-spot radius and  $l$  the mode number. Observe that Eq. (1) indicates that all modes are unstable, with the fastest-growing modes having short wavelengths ( $kL \gg 1$ ) and growth rates  $\gamma_{\text{dec}}(kL \gg 1) = \sqrt{g/L}$ . As described in Ref. 13, the finite-density-gradient scale length is produced by the thermal conduction inside the hot spot. It is shown in this article that mass ablation from the shell's inner surface significantly reduces the deceleration RT growth rates, leading to much lower growth rates than predicted by Eq. (1) and to a cutoff in the unstable spectrum. Mass ablation is caused by the heat flux leaving the hot spot and depositing on the shell's inner surface. We have calculated the ablation velocity and the shell's density-gradient scale length during the deceleration phase. Then, using the RT theory of Ref. 10, we have calculated the growth rates and compared them with the results of numerical simulations. For the direct-drive NIF-like capsule under consideration,<sup>3</sup> the cutoff mode number for the deceleration-phase RT is approximately  $l_{\text{cutoff}} \approx 90$ .

The remainder of this article is divided into two major sections that describe the hot-spot dynamics and the linear stability. The hot-spot model is valid from the beginning of the continuous deceleration phase (after the shock reflection off the shell) until the onset of the ignition process. The evolution of the hot-spot radius, mass, temperature, and density is calculated in terms of initial conditions and hot-spot pressure. The second section is devoted to the hydrodynamic stability analysis of the shell during the continuous deceleration phase. The growth rate of the RT instability is derived, including finite-density-gradient scale length and ablation velocity.

### Hot-Spot Dynamics

The hot spot is a low-density plasma heated by the shock and by the  $PdV$  work of the cold, dense surrounding shell. Its mass is made of the ionized DT gas and the plasma ablated off

the inner shell surface. The hot-spot dynamics is governed by the mass, momentum, and energy conservation equations. The energy equation must include the electronic thermal conduction and alpha-particle energy deposition. Bremsstrahlung radiation energy losses are neglected in this model because they add great complexity to the mathematical solution and their contribution is typically smaller than the mechanical work and/or the fusion power. The magnitude of the radiation losses is larger than the fusion power for temperatures below 4.4 keV, when the  $PdV$  work rate is typically greater than both radiation and fusion power. Thus at such low temperatures both radiation losses and alpha power are negligible with respect to the compression work rate. The  $PdV$  work rate decreases near the shell's stagnation point, where higher temperatures are reached within the hot spot. If such temperatures are well above 4.4 keV, the alpha-particle power is greater than the radiation losses and the bremsstrahlung term can again be neglected in the energy equation. The model described in this section may not apply to capsules that do not ignite or with small ignition margins (small mechanical work rate and low final temperatures) as their evolution can be significantly affected by radiation losses.

This model is expected to predict the main characteristics of the deceleration phase up to the onset of ignition. The actual ignition process in the hot spot is not accurately modeled because the alpha-particle energy is assumed to be locally deposited within the hot spot. Instead, the alpha-particle mean free path is typically of the same order of magnitude as the hot-spot radius, and a fraction of the alpha particles leaves the hot spot and is deposited on the shell's inner surface. Those alpha particles trigger the propagation of a burn wave in the cold, dense shell, which burns until it disassembles. The thermonuclear burn wave propagation is not described by our model and requires a diffusion (or kinetic) treatment of the alpha-particle population. Detailed analysis of the burn wave propagation and the effects of the RT instability on the capsule gain can be found in Ref. 11.

Even though the local deposition approximation used here is strictly valid only when all the alpha particles are absorbed within the hot spot, we artificially include the effect of alpha-particle diffusion by adding a multiplicative factor  $\theta \leq 1$  to the alpha power term. When  $\theta < 1$ , one should also include the alpha power deposited at the inner shell surface due to the  $1-\theta$  fraction of leaking alpha particles. Such a contribution is not included in the derivation of the hot-spot profiles, ablation velocity, and density-gradient scale length because an analytic solution of the conservation equations could not be found.

Thus, an additional limitation of this model is that the fraction of alpha particles leaving the hot spot is small compared to the fraction absorbed.

In conclusion, the model described below is suitable to describe the deceleration phase up to the onset of ignition, but it does not include the relevant physics pertaining to the ignition process or the burn wave propagation. We speculate that most of the RT instability growth occurs before ignition takes place when our model captures the essential physics of the hot-spot dynamics.

### 1. General Equations

The model is based on the Lagrangian form of the equations of motion as the boundary of the hot spot moves before and after stagnation. The Lagrangian equations of motion in spherical geometry can be written in the following form:

$$\frac{1}{\rho} = \frac{1}{3} \frac{\partial r^3}{\partial m}, \quad (2)$$

$$\frac{\partial U}{\partial t} + r^2 \frac{\partial P}{\partial m} = 0, \quad (3)$$

$$c_v \rho^{\Gamma-1} \frac{\partial}{\partial t} \frac{T}{\rho^{\Gamma-1}} = \frac{\partial}{\partial m} \kappa(T) r^4 \rho \frac{\partial T}{\partial m} + \frac{\rho}{4m_i^2} \theta E_\alpha \langle \sigma \mathbf{v} \rangle, \quad (4)$$

where  $c_v = 3/2 A$  is the specific heat at constant volume,  $A = m_i / (1 + Z)$ ,  $m_i$  and  $Z$  are the ion mass and atomic number, respectively ( $Z = 1$  for DT),  $\Gamma$  is the ratio of specific heats or adiabatic index ( $\Gamma = 5/3$  for a monoatomic gas),  $\kappa(T) = \kappa_0 T^\nu$  is the Spitzer thermal conductivity,  $\nu = 5/2$ ,  $E_\alpha = 3.5$  MeV,  $\theta$  is the absorbed alpha-particle fraction, and  $\langle \sigma \mathbf{v} \rangle$  is the fusion reaction rate. The independent variable  $m$  is proportional to the mass within the radius  $r$ :

$$m = \int_0^r \rho(x, t) x^2 dx. \quad (5)$$

Equation (4) has been derived by using the standard ideal gas equation of state  $P = \rho T / A$  and by neglecting bremsstrahlung losses. To solve the conservation equations, we adopt the subsonic flow ordering, which represents a good approximation after the shock transient. We let  $t \sim R / C_s$  (or  $t \sim R / U$ ),  $r \sim R$ , and  $U \sim \epsilon C_s$ , where  $\epsilon \ll 1$  represents the flow Mach number. We find the solution of Eqs. (2)–(4) by a formal

expansion in powers of  $\epsilon$ . By inspection, Eq. (3) reduces to  $\partial_m P = O(\epsilon P/m)$ , yielding

$$P \approx P_{\text{hs}}(t) \quad (6)$$

and reproducing the well-known flat pressure approximation.

The density in the energy equation can be eliminated by using the equation of state, and the fusion rate can be approximated with a quadratic term  $\langle \sigma v \rangle = S_\alpha T^2$ . Such an approximation is valid as long as  $5 < T < 25$  keV, which is a temperature range relevant to ICF ignition experiments. After a straightforward manipulation, the energy equation can be rewritten in the following form:

$$\begin{aligned} c_v \frac{P_{\text{hs}}(t)^{\Gamma-1}}{T^{\Gamma-1}} \frac{\partial}{\partial t} \frac{T^\Gamma}{P_{\text{hs}}(t)^{\Gamma-1}} \\ = A \kappa_0 P_{\text{hs}}(t) \frac{\partial}{\partial m} r^4 T^{\nu-1} \frac{\partial T}{\partial m} + \frac{\theta E_\alpha S_\alpha A}{M_i^2} P_{\text{hs}}(t) T. \end{aligned} \quad (7)$$

Equation (7) can be further simplified by defining the variables  $\Pi \equiv T/P_{\text{hs}}^{1-1/\Gamma}$  and

$$\tau = \frac{3^{4/3}}{A^{1/3}} \frac{\kappa_0}{\Gamma c_v} \int_0^t P_{\text{hs}}(t')^\beta dt' + \tau_0, \quad \beta = \frac{3(\Gamma-1)\nu-1}{3\Gamma}, \quad (8)$$

where  $\tau_0$  is a constant to be determined by the initial conditions. Using Eq. (2) to determine the relation between the volume within the radius  $r$  and  $\Pi$ , one finds

$$r^3 = \frac{3}{A P_{\text{hs}}(t)^{1/\Gamma}} \Phi, \quad \Phi \equiv \int_0^m \Pi(m', \tau) dm', \quad (9)$$

and the energy equation can be rewritten in the following simple form:

$$\frac{\partial \Pi}{\partial \tau} = \frac{\partial}{\partial m} \Pi^{\nu-1} \Phi^{4/3} \frac{\partial \Pi}{\partial m} + \Delta_\alpha \Pi P_{\text{hs}}(t)^\delta, \quad (10)$$

where

$$\delta = \frac{3\nu+1+3\Gamma(1-\nu)}{3\Gamma}, \quad \Delta_\alpha = \left(\frac{A}{3}\right)^{4/3} \frac{\theta E_\alpha S_\alpha}{4\kappa_0 m_i^2}. \quad (11)$$

The next step is to integrate Eq. (10) between 0 and  $m$  and to eliminate  $\Pi$ , leading to the following equation for  $\Phi$ :

$$\frac{\partial \Phi}{\partial \tau} = \Phi^{4/3} \left(\frac{\partial \Phi}{\partial m}\right)^{\nu-1} \frac{\partial^2 \Phi}{\partial m^2} + \Delta_\alpha \Phi P_{\text{hs}}(t)^\delta. \quad (12)$$

Observe that the  $\alpha$  particle term on the right-hand side of Eq. (12) can be combined with the left-hand side by defining the new dependent ( $\Psi$ ) and independent ( $\eta$ ) variables:

$$\Psi = \Phi \exp\left[-D_\alpha \int_{t_0}^t P_{\text{hs}}(t') dt'\right], \quad (13)$$

$$\begin{aligned} \eta = \eta_0 + \frac{3^{4/3} \kappa_0}{A^{1/3} \Gamma c_v} \int_{t_0}^t dt' P_{\text{hs}}(t')^\beta \\ \exp\left[\left(\nu + \frac{1}{3}\right) D_\alpha \int_{t_0}^{t'} P_{\text{hs}}(t'') dt''\right], \end{aligned} \quad (14)$$

where  $t = t_0$  represents the beginning of the continuous deceleration phase,

$$D_\alpha = \frac{\Gamma-1}{4\Gamma} \frac{\theta E_\alpha S_\alpha}{(1+Z)^2}, \quad (15)$$

and  $\eta_0$  is a new constant. After a short calculation, Eq. (12) can be rewritten in the following simple form:

$$\frac{\partial \Psi}{\partial \eta} = \Psi^{4/3} \left(\frac{\partial \Psi}{\partial m}\right)^{\nu-1} \frac{\partial^2 \Psi}{\partial m^2}. \quad (16)$$

A self-similar solution of Eq. (13) can be found by setting

$$\Psi = \left(\frac{a^{-3(\nu+1)}}{\eta^3 [1-\Omega(\nu+1)]}\right)^{\frac{1}{3\nu+1}} F(\xi), \quad \xi = \frac{am}{\eta\Omega}, \quad (17)$$

where  $\xi$  and  $F(\xi)$  are dimensionless and  $a$  is a constant with the dimensions of  $\eta^\Omega/m$  to be determined using the initial conditions. Substituting Eq. (17) into Eq. (16) yields the following ordinary differential equation for  $F(\xi)$ :

$$\frac{3[1-\Omega(\nu+1)]}{3\nu+1}F + \Omega\xi \frac{dF}{d\xi} + F^{4/3} \left( \frac{dF}{d\xi} \right)^{\nu-1} \frac{d^2F}{d\xi^2} = 0. \quad (18)$$

At the hot spot/shell interface, the temperature is considerably less than the central hot-spot temperature. Since the temperature is proportional to  $dF/d\xi$ , one can neglect corrections of the order of  $T_{\text{shell}}/T(r=0)$  and look for solutions of Eq. (18), satisfying  $dF/d\xi = 0$  at the hot-spot radius. The function  $F$  is proportional to the internal energy inside the hot spot and therefore positive by definition. Thus, the solution of Eq. (18) satisfying the boundary conditions can be found only when  $\Omega = 1/(\nu+1)$ , leading to the simplified hot-spot equation

$$\frac{1}{\nu+1}\xi + F^{4/3} \left( \frac{dF}{d\xi} \right)^{\nu-2} \frac{d^2F}{d\xi^2} = 0. \quad (19)$$

The numerical solution of such an equation requires the derivative at  $\xi=0$ ,  $F'(0)$ . It can be easily shown, however, that all the physical quantities are independent of the choice of  $F'(0)$ ; thus, without loss of generality, we set  $F'(0) = 1$ . The solution of Eq. (19) for  $\nu = 5/2$ ,  $F(0) = 0$ , and  $F'(0) = 1$  is shown in Fig. 85.2. Observe that  $dF/d\xi$  (and therefore  $T$ ) vanishes at  $\xi_0 = 1.23$  and  $F(\xi_0) = 0.70$ . Defining the hot spot as the region

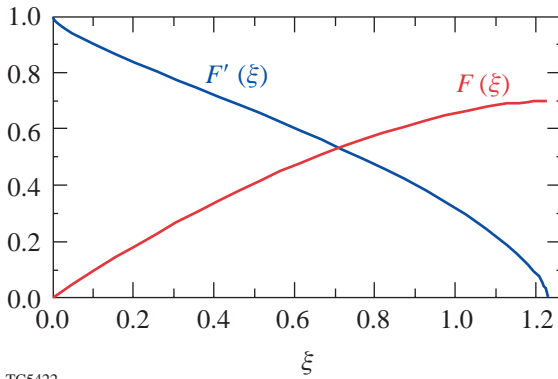


Figure 85.2  
Functions  $F(\xi)$  (proportional to the internal energy) and  $F'(\xi)$  (proportional to the temperature) obtained from the numerical solution of Eq. (19) with  $\nu = 5/2$ ,  $F(0) = 0$ , and  $F'(0) = 1$ . The hot spot is defined to be the region with  $\xi \leq 1.23$ .

with  $\xi \leq \xi_0$  leads to the following expression of the hot-spot mass:

$$M_{\text{hs}} = 4\pi m_{\text{hs}} = 4\pi\xi_0 \eta^{1/(\nu+1)} / a. \quad (20)$$

The constants  $a$  and  $\eta_0$  can be determined from the initial conditions applied to Eqs. (20), (17), and (9), leading to

$$a = \left[ \frac{3F(\xi_0)}{AR_{\text{hs}}(0)^3 P_{\text{hs}}(0)^{1/\Gamma}} \right]^{3(\nu+1)}, \quad \eta_0 = \left[ \frac{aM_{\text{hs}}(0)}{4\pi\xi_0} \right]^{\nu+1}, \quad (21)$$

where  $R_{\text{hs}}(0)$ ,  $P_{\text{hs}}(0)$ , and  $M_{\text{hs}}(0)$  are the initial hot-spot radius, pressure, and mass, respectively. A short calculation using Eqs. (9), (13), (17), and (20) and the equation of state yields the relevant hot-spot parameters [mass, areal density ( $\rho R$ ), density, and temperature] as functions of the hot-spot pressure and radius:

$$M_{\text{hs}}(t) = \left\{ M_{\text{hs}}(0)^{\nu+1} + \chi_0 \kappa_0 A^{\nu+1} \right.$$

$$\left. \int_{t_0}^t P_{\text{hs}}(t')^\beta \left[ R_{\text{hs}}(t')^3 P_{\text{hs}}(t')^{1/\Gamma} \right]^{\nu+1/3} dt' \right\}^{1/(\nu+1)}, \quad (22)$$

$$\rho R \equiv \int_0^{R_{\text{hs}}} \rho dr = \mu_0 \frac{M_{\text{hs}}(t)}{4\pi R_{\text{hs}}(t)^2}, \quad (23)$$

$$\rho_{\text{hs}}(m, t) = \frac{3M_{\text{hs}}(t)}{4\pi R_{\text{hs}}(t)^3} \frac{F(\xi_0)}{\xi_0 F'(\xi)}, \quad (24)$$

$$T_{\text{hs}}(m, t) = \frac{AP_{\text{hs}}(t)}{\rho_{\text{hs}}(m, t)},$$

where

$$\chi_0 \equiv \frac{\Gamma-1}{\Gamma} \frac{3^{1-\nu} (4\pi\xi_0)^{\nu+1}}{F(\xi_0)^{\nu+1/3}}, \quad (25)$$

$$\mu_0 = \frac{F(\xi_0)^{2/3}}{\xi_0} \int_0^{\xi_0} \frac{d\xi}{F(\xi)^{2/3}}.$$

For  $\nu = 5/2$  and  $\Gamma = 5/3$ , we find  $\mu_0 = 2.27$  and  $\chi_0 = 3052.8$ . Observe that the hot-spot mass increases with time at a rate that depends on the thermal conductivity coefficient. The mass increase is due to the ablation off the shell's inner surface. The hot-spot radius and pressure are related through Eq. (9), which can be rewritten by using the initial conditions, leading to

$$\frac{R_{\text{hs}}(t)^3}{R_{\text{hs}}(0)^3} = \left[ \frac{P_{\text{hs}}(0)}{P_{\text{hs}}(t)} \right]^{1/\Gamma} \exp \left[ D_\alpha \int_{t_0}^t P_{\text{hs}}(t) \right]. \quad (26)$$

In the absence of alpha-particle heating ( $D_\alpha = 0$ ), Eq. (26) yields  $P_{\text{hs}} R_{\text{hs}}^{3\Gamma} = \text{constant}$ , indicating that the hot spot behaves like a closed system that is adiabatically heated ( $PV^\Gamma = \text{constant}$ , where  $V$  is the volume). This result is somewhat surprising because the hot spot is not a closed system since its mass increases with time. From the energetic point of view, however, the hot spot is indeed insulated as the heat conduction losses are recycled into the hot spot via the ablated shell material. This can be shown by writing the total (internal + kinetic) energy equation in the conservative form:

$$\begin{aligned} & \frac{\partial}{\partial t} \left( \frac{P}{\Gamma-1} + \rho \frac{U^2}{2} \right) + \nabla \cdot \left[ \mathbf{v} \left( \frac{\Gamma P}{\Gamma-1} + \rho \frac{U^2}{2} \right) \right] \\ & = \nabla \cdot \kappa(T) \nabla T + \frac{\rho^2}{4M_i^2} \theta E_\alpha \langle \sigma \mathbf{v} \rangle. \end{aligned} \quad (27)$$

Using the subsonic flow assumption, we neglect the hot-spot kinetic energy with respect to the internal energy. Then, after approximating the fusion cross section with the quadratic form  $\langle \sigma \mathbf{v} \rangle \approx S_\alpha T^2$ , Eq. (27) is integrated over the hot-spot volume enclosed by the inner shell surface. At the inner surface, the shell material is cold and the thermal conduction can be neglected. A straightforward calculation leads to the following form of the energy equation:

$$\begin{aligned} & \frac{d}{dt} (P_{\text{hs}} R_{\text{hs}}^3) + 3R_{\text{hs}}^2 P_{\text{hs}} \left[ \Gamma U(R_{\text{hs}}, t) - \frac{dR_{\text{hs}}}{dt} \right] \\ & = \Gamma D_\alpha P_{\text{hs}}^2 R_{\text{hs}}^3, \end{aligned} \quad (28)$$

where  $U(R_{\text{hs}}, t)$  is the flow velocity at the shell's inner surface. The flow velocity results from the combination of the inner

surface motion and the ablative flow:

$$U(R_{\text{hs}}, t) = \dot{R}_{\text{hs}} - V_a, \quad (29)$$

where  $V_a$  is the ablation velocity and  $\dot{R}_{\text{hs}}$  scales with the implosion velocity. Since  $V_a \ll \dot{R}_{\text{hs}}$ , the ablation velocity can be neglected, and Eq. (28) yields the exact solution shown in Eq. (26). Thus, Eqs. (26) and (28) are equivalent forms of the energy equation. Notice that the heat conduction losses do not enter into the global energy balance of the hot spot. This is because the heat flux leaving the hot spot is deposited onto the shell's inner surface. A fraction of this energy is transformed into internal energy of the shell material ablating into the hot spot. The remaining fraction produces the  $PdV$  work done by the ablated plasma entering the hot spot against the hot-spot pressure. In other words, the energy leaving the hot spot in the form of heat conduction losses goes back into the hot spot in the form of internal energy and compression work of the ablated plasma. Therefore, conduction losses are not real energy losses and do not affect the global energy balance of the hot spot as shown by Eq. (28). It is important to emphasize that the hot-spot energy is proportional to its pressure and the conduction losses affect the hot-spot temperature but not its pressure. This conclusion implies that greater heat conduction losses would lower the temperature and raise the density (through larger ablation at the shell's inner surface), leaving the pressure ( $P \sim \rho T$ ) unaltered.

Equation (26) relates hot-spot radius and pressure. All the hydrodynamic quantities shown in Eqs. (22)–(24) can therefore be expressed as functions of the pressure only, using Eq. (26). It follows that a fully self-consistent implosion model requires additional equations relating  $P_{\text{hs}}(t)$  to the shell's properties. The coupling between the hot spot and the shell will be discussed in a forthcoming LLE Review. Here, we consider  $P_{\text{hs}}$  as a given function of time and use the hot-spot analysis developed in this section to determine the ablation velocity and density-gradient scale length.

## 2. Ablation Velocity and Density-Gradient Scale Length

An important result of the analysis carried out in the previous section concerns the hot-spot mass. Equation (22) shows that the hot-spot mass increases with time. Its rate of increase depends on the magnitude of the heat conduction coefficient  $\kappa_0$  [here,  $\kappa(T) = \kappa_0 T^\nu$ ] and the hot-spot pressure. The ablation velocity at the shell's inner surface follows by noticing that the mass ablation rate off the shell,  $\dot{M}_a$ , must equal the rate of change of the hot-spot mass  $\dot{M}_{\text{hs}}$ . Given the

hot-spot radius  $R_{\text{hs}}$  and the shell's peak density  $\rho_{\text{shell}}$ , the ablation rate is  $\dot{M}_a = 4\pi R_{\text{hs}}^2 \rho_{\text{shell}} V_a$ , where  $V_a$  is the ablation velocity. Thus setting  $\dot{M}_a = \dot{M}_{\text{hs}}$  yields the ablation velocity

$$V_a = \frac{\dot{M}_{\text{hs}}}{4\pi R_{\text{hs}}^2 \rho_{\text{shell}}}, \quad (30)$$

where  $\dot{M}_{\text{hs}}$  can be determined from Eq. (22). Then, using the  $m$ -derivative of  $\Phi$  to relate  $T$  and  $\eta$ , the ablation velocity can be written in terms of standard hot-spot and shell parameters

$$V_a = \frac{3(\Gamma-1)}{(\nu+1)\Gamma} \frac{\xi_0}{F'(0)^\nu F(\xi_0)^{1/3}} \frac{A\kappa_0 T_{\text{hs}}(0,t)^\nu}{\rho_{\text{shell}}(t) R_{\text{hs}}(t)}, \quad (31)$$

where both the central hot-spot temperature and radius depend only on the hot-spot pressure. Using  $F'(0) = 1$  and  $\nu = 5/2$  to solve Eq. (18) leads to  $\xi_0 = 1.23$ ,  $F(\xi_0) = 0.7$ . The ablation velocity can then be calculated using standard ICF units, leading to the following simple form:

$$V_a (\mu\text{m/ns}) = 6 \times 10^3 \frac{(T_{\text{keV}}^{\text{hs}})^{5/2}}{R_{\mu\text{m}}^{\text{hs}} \rho_{\text{g/cm}^3}^{\text{shell}} \Lambda^{\text{hs}}}, \quad (32)$$

where  $R^{\text{hs}}$ ,  $T^{\text{hs}}$ , and  $\Lambda^{\text{hs}}$  are the hot-spot radius in  $\mu\text{m}$ , central temperature  $g$  in keV, and Coulomb logarithm, and  $\rho^{\text{shell}}$  is the shell's peak density in  $\text{g/cm}^3$ . Figure 85.3 shows the temporal evolution of the ablation velocity for a direct-drive NIF cap-

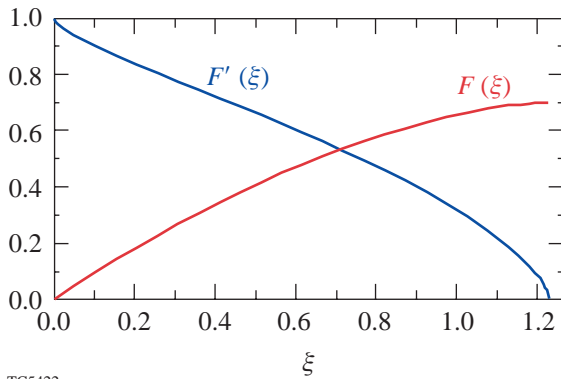


Figure 85.3  
Evolution of the ablation velocity at the shell's inner surface of a NIF-like capsule as predicted by Eq. (32) (dashed) and the result of numerical simulations (solid).

sule obtained from Eq. (32) and the result of numerical simulations using  $\Lambda^{\text{hs}} = 5$ .

In addition to the ablative stabilization, the RT growth rates are reduced by the well-known finite-density-gradient effects. Since the ablative flow at the inner shell surface is subsonic, the minimum density-gradient scale length can be calculated using the well-known isobaric model<sup>14</sup> characterized by the following approximate form of the energy equation:

$$\nabla \cdot \left[ \mathbf{v} \frac{\Gamma P_{\text{hs}}(t)}{\Gamma-1} - \kappa \nabla T \right] = 0. \quad (33)$$

Integrating Eq. (33) and using the continuity of the mass flow ( $\rho U = \text{constant}$ ) leads to the following ordinary differential equation for the density profile near the shell's inner surface:

$$\frac{1}{\hat{\rho}} \frac{\partial \hat{\rho}}{\partial r} = \hat{\rho}^\nu \frac{(1-\hat{\rho})}{L_0}, \quad (34)$$

where  $\hat{\rho} = \rho/\rho_{\text{shell}}$  is the density normalized to the peak density in the shell ( $\rho_{\text{shell}}$ ) and

$$L_0 = \frac{\Gamma-1}{\Gamma} \frac{A\kappa(T_{\text{shell}})}{\rho_{\text{shell}} V_a}. \quad (35)$$

Here  $T_{\text{shell}} = AP_{\text{hs}}(t)/\rho_{\text{shell}}$  represents the temperature calculated at the peak of the density. Equation (35) is valid only near the shell's inner surface within a distance of the order of the length  $L_0$ . The minimum value of the density-gradient scale length ( $L_m$ ) can be determined by setting to zero the radial derivative of Eq. (34). A straightforward manipulation yields

$$L_m = L_0 \frac{(\nu+1)^{\nu+1}}{\nu^\nu}. \quad (36)$$

Using  $\nu = 5/2$  in Eq. (36) and substituting Eq. (32) into Eq. (35) leads to the following simple expression of the density-gradient scale length:

$$L_m = 6.8 R_{\text{hs}} [AP_{\text{hs}}(t)/\rho_{\text{shell}} T_{\text{hs}}(0,t)]^{5/2}, \quad (37)$$

where  $P_{\text{hs}}(t)$  is the hot-spot pressure. Figure 85.4 shows the temporal evolution of  $L_m$  calculated from Eq. (37) and from the

numerical simulations of a NIF direct-drive capsule. Observe that the density-gradient scale length is quite smaller than the hot-spot radius, implying that its stabilizing effects will impact only short-wavelength modes (large  $l$ -mode numbers).

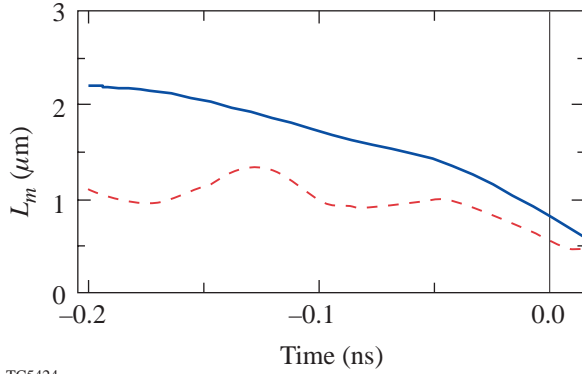


Figure 85.4 Evolution of the density-gradient scale length at the shell's inner surface of a NIF-like capsule as predicted by Eq. (37) (dashed) and the result of numerical simulations (solid).

In the next section, the theory developed in the **General Equations** section is used to calculate the hydrodynamic profiles inside the hot spot and to show how the profiles are affected by the ablation process.

### 3. Hot-Spot Profiles

The density, temperature, and velocity profiles inside the hot spot can be determined easily from the theory developed in the **Hot-Spot Dynamics** section. The theory is based on the solution of the gas dynamic equations in a Lagrangian form with  $m, t$  as independent variables. All the spatial profiles are described by the function  $F(\xi)$ , where  $\xi = am/\eta^{2/7}$  for  $\nu = 5/2$ . Instead of the variable  $\xi$ , a more convenient expression of the profiles should make use of the spatial coordinate  $\hat{r} \equiv r/R_{\text{hs}}(t)$ . The relation between  $\hat{r}$  and  $\xi$  can be found by rewriting Eq. (9) using Eqs. (26), (17), and (21). A simple manipulation yields the following relation:

$$\hat{r}^3 = \frac{F(\xi)}{F(\xi_0)}. \quad (38)$$

All the spatial hot-spot profiles for  $\nu = 5/2$  can be found by inverting Eq. (38) and finding  $\xi$  in terms of  $\hat{r}$ ; however, since  $F(\xi)$  is not analytical, the inversion must be carried out numerically, leading to the following approximation for  $\xi$  and  $F'(\xi)$ :

$$\xi \approx \xi_0 \left\{ 1 - [1 - \hat{r}^3]^{3/5} \right\}, \quad (39)$$

$$F'(\xi) \approx \frac{(1 - \hat{r}^2)^{2/5}}{1 - 0.15 \hat{r}^2}. \quad (40)$$

The hot-spot temperature profile follows immediately from Eq. (24) and Eq. (40) leading to

$$T_{\text{hs}}(r, t) \approx T_{\text{hs}}(0, t) \frac{(1 - \hat{r}^2)^{2/5}}{1 - 0.15 \hat{r}^2}. \quad (41)$$

When compared with the commonly used profile<sup>1</sup>  $T_c = T_0(1 - \hat{r}^2)^{2/7}$ , Eq. (41) is in very good agreement except near the boundary of the hot spot  $\hat{r} \approx 1$ . The different behavior near the hot-spot boundary is relevant to the calculation of the heat flux leaving the hot spot, which is proportional to  $[T^{5/2} d_r T]_{\hat{r}=1}$ . The common profile with the power  $2/7$  yields a finite heat flux while the profile given by Eq. (41) yields zero flux. Since the hot-spot boundary represents the cold shell's inner surface, the heat flux cannot propagate through the shell because the heat conductivity is negligible throughout the shell material. The correct temperature profiles must therefore produce a vanishing heat flux at the hot-spot boundary as indicated by Eq. (41). As mentioned in the **General Equations** section, the heat flux is absorbed on the shell's inner surface by the material that ablates into the hot spot.

The hot-spot density profile follows from Eq. (41) and the isobaric assumption, leading to

$$\rho_{\text{hs}}(r, t) \approx \rho_{\text{hs}}(0, t) \frac{1 - 0.15 \hat{r}^2}{(1 - \hat{r}^2)^{2/5} + \epsilon}, \quad (42)$$

where the *ad hoc* term  $\epsilon \equiv 0.85 \rho_{\text{hs}}(0, t) / \rho_{\text{shell}} \ll 1$  has been included to remove the singularity at  $\hat{r} = 1$ , which arises from the zero shell temperature approximation used to solve the hot-spot equation [Eq. (16)].

The velocity profile can be determined from the Lagrangian equation  $u = \partial_r r$  and Eq. (9). Using the definition of the ablation velocity given in Eq. (30), the hot-spot velocity profile has the form

$$u(r,t) = \hat{r} \dot{R}_{\text{hs}} - \frac{\xi(\hat{r})}{\xi_0} \frac{\rho_{\text{shell}}}{\rho_{\text{hs}}(r,t)} \frac{V_a}{\hat{r}^2}, \quad (43)$$

where  $\xi(\hat{r})$  and  $\rho_{\text{hs}}(r,t)$  are given in Eqs. (38) and (43), respectively. During the deceleration phase, the velocity is negative (i.e., directed in the negative  $r$ -direction) and the velocity profile has a minimum (i.e., a maximum for the absolute value of  $u$ ) due to the blowoff of the material ablated off the shell [the second term in Eq. (43)]. The minimum occurs at the radial position

$$\hat{r}_{\text{min}} \approx \frac{1 + 0.6 \hat{V}_b}{1 + 0.72 \hat{V}_b}, \quad (44)$$

where  $\hat{V}_b = \rho_{\text{shell}} V_a / \rho_{\text{hs}}(0,t) |\dot{R}_{\text{hs}}|$ . Near stagnation,  $\hat{V}_b \gg 1$ ,  $\hat{r}_{\text{min}} \approx 0.8$ , and the velocity at the point of minimum is approximately

$$u(\hat{r}_{\text{min}}, t) \approx 0.8 \dot{R}_{\text{hs}} - 0.6 V_a \frac{\rho_{\text{shell}}}{\rho_{\text{hs}}(r_{\text{min}}, t)}, \quad (45)$$

where  $\rho_{\text{hs}}(\hat{r}_{\text{min}}, t) \approx 1.46 \rho_{\text{hs}}(0, t)$  is the density at the location of minimum velocity. Observe that Eq. (45) is a useful tool for calculating the ablation velocity near stagnation from the numerical simulations because the velocity  $u_{\text{min}} = u(\hat{r}_{\text{min}}, t)$ , and the densities  $\rho_{\text{hs}}(\hat{r}_{\text{min}}, t)$  and  $\rho_{\text{shell}}$  can be easily determined from the codes' output, while  $\dot{R}_{\text{hs}}$  is small and can be neglected.

### Growth Rates of the Deceleration RT Instability

During the continuous deceleration phase after the interaction of the shell with the return shock, the shell's inner surface is unstable to the RT instability and any small perturbation in the hydrodynamic quantities would grow rapidly. The general formula derived in Ref. 10 yields the growth rate of the ablative RT as a function of the ablation velocity  $V_a$ , the shell deceleration  $g$ , the power index for thermal conduction  $\nu = 5/2$ , and the mode wave number  $k \approx l/R_{\text{hs}}$  for  $l \gg 1$ . Since all such quantities are functions of time, the exponential growth of the linear perturbation occurs for sufficiently large  $l$ 's only when the typical growth time is shorter than the characteristic time scale of the one-dimensional evolution. In order to verify the theoretical results, we have carried out several 2-D single-mode simulations.

The 1-D code *LILAC*'s<sup>15</sup> output for the NIF-like capsule at 9.3 ns, characterizing the beginning of the coasting phase, was later used as input for a high-resolution Eulerian hydrocode.<sup>16</sup> The latter solves the single fluid mass, momentum, and energy equations, including Spitzer conduction, local alpha deposition, and bremsstrahlung on a very fine grid. The high resolution is needed to correctly simulate the growth of short-wavelength modes on the shell's inner surface. Aside from the bremsstrahlung losses, the code solves the same single fluid model on which the theory is based, providing a robust check of the theoretical results. The RT evolution is investigated by introducing a small-amplitude, 2-D perturbation of the hydrodynamic variables at about 200 ps before stagnation when the continuous deceleration phase begins.

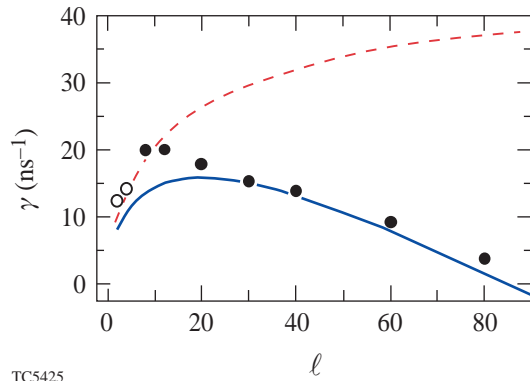
For a direct-drive NIF-like capsule the deceleration phase occurs over an interval of approximately 200 ps. During that time (see Fig. 85.1) the deceleration varies from a few hundreds  $\mu\text{m}/\text{ns}^2$  to about 4000  $\mu\text{m}/\text{ns}^2$ , the ablation velocity increases from  $\sim 13$  to  $\sim 25$   $\mu\text{m}/\text{ns}$ , the density-gradient scale length varies between 1 to 2  $\mu\text{m}$ , and the hot-spot radius reduces from 100  $\mu\text{m}$  to about 55  $\mu\text{m}$ . The RT growth becomes significant during the last 100 ps before stagnation when the acceleration is large, and the hot-spot radius decreases from 75 to 55  $\mu\text{m}$ . The growth rate of large  $l$  modes can be determined using the planar results of Ref. 10 derived for the acceleration-phase RT. For a NIF-like capsule during the continuous deceleration phase in the 100-ps interval before stagnation  $\langle g \rangle \approx 3100$   $\mu\text{m}/\text{ns}^2$ ,  $\langle V_a \rangle \approx 18$   $\mu\text{m}/\text{ns}$ ,  $\langle L_m \rangle \approx 1.5$   $\mu\text{m}$ , and  $\langle R_{\text{hs}} \rangle \approx 65$   $\mu\text{m}$ , leading to a Froude number  $Fr \approx 0.5$ , where  $Fr = V_a^2 / g L_0$  and  $L_0 = 0.12 L_m$ . Using Eq. (23) and Fig. 6 of Ref. 7, we determine the appropriate growth-rate formula:

$$\gamma = 0.9 \sqrt{\frac{k \langle g \rangle}{1 + k \langle L_m \rangle}} - 1.4 k \langle V_a \rangle, \quad (46)$$

where  $k = l/R_{\text{hs}}$  for large  $l$ 's.

Figure 85.5 compares the unstable spectrum calculated using Eq. (46) with  $R_{\text{hs}} = 65$   $\mu\text{m}$ , the classical RT spectrum without ablation [Eq. (1) with  $L = L_m$ ], and the results of numerical simulations. Except for  $l = 2, 4$  (open circles), the numerical growth rates are calculated in the 100-ps time interval before stagnation. The simulations of modes  $l = 2, 4$  (open circles) show a clear exponential growth only after the shell stagnation time, and their numerical growth rate is calcu-

lated during the 50-ps interval after stagnation. It is important to observe that the planar theory agrees well with the numerical results only for  $l \geq 20$ . Low  $l$  modes seem to grow faster (almost classically) than predicted by Eq. (46), indicating that convergence effects may reduce the ablative stabilization at low  $l$ . Furthermore, Fig. 85.5 shows that the finite ablation velocity off the shell's inner surface induces a cutoff in the RT unstable spectrum, suppressing short-wavelength modes with  $l > 90$ .



TC5425

Figure 85.5

Growth rate versus mode number for the deceleration-phase RT of a NIF-like capsule as predicted by this work [Eq. (46) (solid)], by the classical fitting formula [Eq. (1)] with  $L = L_m$  (dashed), and by the results of numerical simulations (open circles). The classical formula overestimates the growth rate of the instability for  $l \gtrsim 10$ .

## Conclusion

In conclusion, an analytic model of the hot-spot dynamics has been developed, and all hot-spot profiles and hydrodynamic quantities relevant to the deceleration-phase instability have been determined. We have shown that the ablative flow off the shell's inner surface plays a crucial role in reducing the growth rate and suppressing short-wavelength modes in the deceleration-phase RT instability. The ablation velocity and the density-gradient scale length have been calculated in terms of standard hot-spot parameters. Using the theory of Ref. 10, the growth rate formula has been determined. Detailed numerical simulations have confirmed the theoretical results and have shown RT suppression at short wavelengths. Calculations of the unstable spectrum of a direct-drive NIF-like capsule<sup>3</sup> during the deceleration phase have indicated that the instability is suppressed for mode numbers  $l > 90$ .

## ACKNOWLEDGMENT

This work was supported by the U.S. Department of Energy Office of Inertial Confinement Fusion under Cooperative Agreement No. DE-FC03-92SF19460, the University of Rochester, and the New York State Energy Research and Development Authority. The support of DOE does not constitute an endorsement by DOE of the views expressed in this article.

## REFERENCES

1. J. D. Lindl, *Inertial Confinement Fusion: The Quest for Ignition and Energy Gain Using Indirect Drive* (Springer-Verlag, New York, 1998).
2. T. R. Dittrich *et al.*, Phys. Plasmas **6**, 2164 (1999).
3. Laboratory for Laser Energetics LLE Review **79**, 121, NTIS document No. DOE/SF/19460-317 (1999). Copies may be obtained from the National Technical Information Service, Springfield, VA 22161.
4. S. E. Bodner, Phys. Rev. Lett. **33**, 761 (1974).
5. H. Takabe *et al.*, Phys. Fluids **28**, 3676 (1985).
6. J. Sanz, Phys. Rev. Lett. **73**, 2700 (1994).
7. R. Betti, V. N. Goncharov, R. L. McCrory, P. Sorotokin, and C. P. Verdon, Phys. Plasmas **3**, 2122 (1996).
8. V. N. Goncharov, R. Betti, R. L. McCrory, P. Sorotokin, and C. P. Verdon, Phys. Plasmas **3**, 1402 (1996).
9. V. N. Goncharov, R. Betti, R. L. McCrory, and C. P. Verdon, Phys. Plasmas **3**, 4665 (1996).
10. R. Betti, V. N. Goncharov, R. L. McCrory, and C. P. Verdon, Phys. Plasmas **5**, 1446 (1998).
11. R. Kishony, "Ignition Criterion in Inertial Confinement Fusion Using Self-Similar Solutions, and the Effect of Perturbations on Ignition," Ph.D. thesis, Tel Aviv University, 1999.
12. F. Hattori, H. Takabe, and K. Mima, Phys. Fluids **29**, 1719 (1986).
13. M. Murakami, M. Shimoide, and K. Nishihara, Phys. Plasmas **2**, 3466 (1995).
14. H. J. Kull, Phys. Fluids B **1**, 170 (1989).
15. J. Delettrez and E. B. Goldman, Laboratory for Laser Energetics Report No. 36, University of Rochester (1976); also NTIS document No. DOE/SF/19460-118. Copies may be obtained from the National Technical Information Service, Springfield, VA 22161.
16. V. A. Lobatchev, "Hydrodynamics of Inertial Fusion Capsules: Feedout and Deceleration Phase Instability," Ph.D. thesis, University of Rochester, 2000.